Wall accumulation and spatial localization in particle-laden wall flows

G. Sardina[1], P. Schlatter[2], L. Brandt[2], F. Picano[1] and C. M. Casciola[1]†

[1] Dipartimento di Ingegneria Meccanica e Aerospaziale, Sapienza University of Rome, 00184 Rome, Italy

[2] Linné FLOW Center, KTH Mechanics, SE-100 44 Stockholm, Sweden

We study the two main phenomenologies associated with the transport of inertial particles in turbulent flows, turbophoresis and small-scale clustering. Turbophoresis describes the turbulence-induced wall accumulation of particles dispersed in wall turbulence, while small-scale clustering is a form of local segregation that affects the particle distribution in the presence of fine-scale turbulence. Despite the fact that the two aspects are usually addressed separately, this paper shows that they occur simultaneously in wall-bounded flows, where they represent different aspects of the same process. We study these phenomena by post-processing data from a direct numerical simulation of turbulent channel flow with different populations of inertial particles. It is shown that artificial domain truncation can easily alter the mean particle concentration profile, unless the domain is large enough to exclude possible correlation of the turbulence and the near-wall particle aggregates. The data show a strong link between accumulation level and clustering intensity in the near-wall region. At statistical steady state, most accumulating particles aggregate in strongly directional and almost filamentary structures, as found by considering suitable two-point observables able to extract clustering intensity and anisotropy. The analysis provides quantitative indications of the wall-segregation process as a function of the particle inertia. It is shown that, although the most wall-accumulating particles are too heavy to segregate in homogeneous turbulence, they exhibit the most intense local small-scale clustering near the wall as measured by the singularity exponent of the particle pair correlation function.

Key words: particle/fluid flow, turbulence simulation, turbulent mixing

---

1. Introduction

Industrial devices and environmental processes often involve the motion of a dispersed phase in a flow. Particulate dust impinging on turbine blades or walls of combustion chambers may negatively affect the efficiency of these systems. For instance, in the aeronautical context, the ash generated in volcanic eruptions can induce problems in aeroplane components, calling for accurate description of dust transport to determine conditions for critical failures. Transport of inertial particles in turbulent flows is characterized by the peculiar phenomenologies of small-scale

† Email address for correspondence: carlomassimo.casciola@uniroma1.it

clustering and turbophoresis – see, among others, Toschi & Bodenschatz (2009) and Balachandar & Eaton (2010) for recent reviews. It is important to underline that, while small-scale clustering occurs in both homogeneous and inhomogeneous flow configurations, turbophoresis is a distinctive feature of particle dispersion in wall-bounded flows.

Small-scale clustering consists of loss of spatial homogeneity of the particle distribution due to the combination of particle inertia and turbulence. As a result, a multi-scale distribution of local particle concentration is produced, leading to the formation of particle clusters and corresponding void regions. Though their origin is still debated, one of the most credited and simple explanations of these anomalous features is particle inertia selectively filtering suitable turbulent excitations, at least partially. Actually, inertia prevents particles from following convoluted fluid trajectories leading to preferential concentration outside such vortical structures. One of the first numerical observations of the correlation between particle localization and vorticity field was based on a direct numerical simulation (DNS) of a homogeneous isotropic configuration (Squires & Eaton 1991). The ratio between peak concentration and average value was found to be of order 30, with particles mainly localized in elliptic regions outside vortices. The main parameter controlling clustering is the Stokes number based on the Kolmogorov time scale (Wang & Maxey 1993), implying that the clustering dynamics is essentially controlled by small-scale turbulent motions. The clustering is maximum when the characteristic Kolmogorov–Stokes number is of order one, as successively confirmed by a number of numerical simulations and experiments (see e.g. Bec *et al.* 2007). From the theoretical point of view, Elperin, Kleeorin & Rogachevskii (1996) used a path-integral approach in order to obtain an equation for the particle density correlation function, observing that the particle distribution is strongly intermittent when the particle inertia is large enough.

A number of observables can be used to quantify clustering. Fessler, Kulick & Eaton (1994) measured particle clustering in the bulk of a particle-laden channel flow by means of the so-called clustering index, which parametrizes the deviation of the actual particle distribution from the corresponding random Poisson distribution. One of the most powerful observables is the radial distribution function (RDF), introduced in Sundaram & Collins (1997) to address particle clustering in homogeneous turbulence by means of Lagrangian–Eulerian DNS. The RDF is related to the probability of finding a particle pair at a certain radial distance and behaves at small scales as a power law. The scaling exponent is related to the dimension of the fractal set supporting the particle distribution, as discussed by Bec *et al.* (2007), and can be used to measure small-scale clustering. In the paper by Calzavarini *et al.* (2008), a new clustering indicator, based on the Kolmogorov distance between two distributions, is introduced to measure the particle clustering in heterogeneous particle-laden flows. More recently, the Voronoï tessellation analysis was used to quantify the particle preferential concentration in particle-laden grid turbulence (see Monchaux, Bourgoin & Cartellier 2010). This global analysis allows the structures of the particle clusters and void regions to be addressed.

Since the divergence of the particle velocity is related to the divergence of the particle acceleration field, many recent experiments have focused on measuring particle accelerations in a variety of turbulent flows – see Ayyalasomayajula *et al.* (2006) for grid turbulence and Gerashchenko *et al.* (2008) for boundary layers. More recently, Gualtieri, Picano & Casciola (2009) addressed the anisotropy of particle distributions in homogeneous shear flow, by using the angular distribution function (ADF); this extends the concept of the RDF while keeping the dependence on direction. These

authors showed that small-scale clustering is strongly anisotropic also at the small scales where the carrier phase velocity field already reaches the isotropic regime associated with the direct Kolmogorov cascade.

Despite the vortical centrifuge effect being the most popular explanation of clustering, other mechanisms have been proposed. In fact, particle clustering is present also in random flows without coherent vortical structures (Mehlig *et al.* 2005). In particular, Goto & Vassilicos (2008) and Coleman & Vassilicos (2009) proposed the sweep–stick mechanism for particle clustering, consisting of preferential accumulation in stagnation points of fluid acceleration.

The other peculiar aspect of inertial particles in turbulence is turbophoresis in wall flows. Turbophoresis amounts to a net particle flux towards the wall, where it induces a peak in average concentration. One of the first theoretical studies on turbophoresis was conducted by Caporaloni *et al.* (1975), with extensive further investigations described in Reeks (1983), where the net particle flux towards the wall was related to the skewness of the particle velocity distribution. The phenomenology has been investigated experimentally in a number of papers (see e.g. Kaftori, Hetsroni & Banerjee 1995*a*,*b*; Niño & Garcia 1996; Righetti & Romano 2004). More recently, turbophoresis has been addressed by means of DNS in channel and pipe flow configurations. Inertial particles seem to be preferentially localized in wall regions with instantaneous streamwise velocity deficit (see Eaton & Fessler 1994; Pan & Banerjee 1996). Rouson & Eaton (2001) found a strong link between particle accumulation and turbulent wall structures. In particular, sweep and ejection events control particle transfer to the wall, as found in the theoretical works of Young & Leeming (1997) and Cerbelli, Giusti & Soldati (2001). Subsequently, Marchioli & Soldati (2002) and Picciotto, Marchioli & Soldati (2005) showed a strong correlation between coherent wall structures, preferential particle accumulation and deposition that causes particles to stay near the wall in the region of slower fluid. All these simulations assume particle motions to be periodic in the streamwise direction. To address the spatial evolution, Picano, Sardina & Casciola (2009) consider the DNS of a spatially developing particle-laden turbulent pipe flow. In this case the particle preferential localization in ejection events is a necessary condition in order to reach the equilibrium particle concentration.

Clustering quantification (RDF) at a distance corresponding to one particle diameter and turbophoresis (mean particle concentration) are combined in the expression for the particle collision rate (Sundaram & Collins 1997):

$$N_c = \pi c^2 \sigma^2 g_0(\sigma) \langle \delta v_p(\sigma) | \delta v_p < 0 \rangle, \qquad (1.1)$$

where N_c is the total collision rate, c is the mean concentration, g_0 is the RDF, σ is the length scale characteristic of the collision (typically the diameter of mono-disperse particles) and $\langle \delta v_p(\sigma) | \delta v_p < 0 \rangle$ is the spherical average of the mean relative velocity of collision. RDF and mean particle concentration are not dynamically independent because, as will be shown, a strong interaction exists between clustering and turbophoresis.

The aim of the present work is to investigate the connections between these two phenomena. In order to address these issues, data of a DNS of a particle-laden periodic turbulent channel flow at $Re_\tau = 180$ are analysed. We address possible confinement and blocking effects by comparing two simulations: one in a standard domain ($4\pi \times 2 \times 4/3\pi$), and the other in a large domain ($12\pi \times 2 \times 4\pi$). The latter domain size is the largest the authors are aware of concerning the simulation of turbulent flows transporting a dispersed phase. For turbulent unladen flows, it is

known that small domains can artificially modify the turbulent kinetic energy, which is mainly associated with large structures, whereas the mean flow appears to be less affected – see del Álamo & Jiménez (2003) for turbulent channel flow. We will show instead that, for the dispersed phase, significant alterations already appear in the mean particle concentration profile. Presumably, the strong sensitivity of the particle concentration to domain truncation is induced by the finite relaxation time, which lets the particles perceive the space–time correlation of the fluid velocity field. Actually, our data indicate that single-point probability density functions (p.d.f.s) of fluid velocity, particle velocity and fluid velocity conditioned to particles are essentially unaffected by domain truncation, while two-point fluid correlations are significantly altered when the domain dimensions are insufficient.

We will further show that the clustering intensity in the near-wall region is directly correlated with the strength of the turbophoretic drift. In this region, clustering is largely different from the standard homogeneous and isotropic paradigm: the clusters feature a strong directional orientation, and clustering is much more intense. Physically, this behaviour is explained by recalling that, to reach equilibrium distribution, the particles must balance the turbophoretic drift by localizing into events with outward fluid velocity. Technically, the analysis is performed by considering the ADF and the small-scale behaviour of the RDF, which is quantitatively evaluated by the scaling exponent related to the fractal dimension of the geometrical structure of the particle distribution.

The paper is organized as follows. Section 2 introduces the numerical methodology. The results are discussed in § 3. The main conclusions are condensed in § 4.

2. Numerical methodology

A coupled Eulerian–Lagrangian numerical method has been used to perform the numerical simulations of the particle-laden turbulent channel flow described in this paper.

We assume the following simplifying hypothesis for the dispersed phase: every particle is considered to be a rigid sphere with diameter much smaller than the viscous scales of the turbulence. We consider a dilute suspension with ratio of particle density to fluid density of the order of 10^3, as appropriate, for example, for a solid phase dispersed in air. With the previous assumptions, the only significant force acting on the particles in the absence of gravity is the viscous Stokes drag, while particle feedback on the carrier phase, inter-particle collisions and hydrodynamic coupling between particles can be neglected (Maxey & Riley 1983).

Under these conditions (assuming one-way coupling regime), the carrier fluid is governed by the classical non-dimensional incompressible Navier–Stokes equations,

$$\nabla \cdot \boldsymbol{u} = 0, \tag{2.1}$$

$$\frac{\partial \boldsymbol{u}}{\partial t} + \boldsymbol{u} \cdot \nabla \boldsymbol{u} = -\nabla p + \frac{1}{Re} \nabla^2 \boldsymbol{u}, \tag{2.2}$$

where $\boldsymbol{u}(\boldsymbol{x}, t)$ is the fluid velocity and p is the pressure. As far as the carrier flow is concerned, the only control parameter is the Reynolds number, $Re = U_c h / \nu$, with h the channel half-width, U_c the centreline velocity of the corresponding laminar Poiseuille profile with the same mass flux of the actual turbulent flow, and ν the kinematic viscosity. In turbulent wall-bounded flows, it is common to refer to the so-called friction Reynolds number $Re_\tau = U_* h / \nu$, where $U_* = \sqrt{\tau_w / \rho}$ is the friction velocity related to the shear stress at the wall τ_w and ρ is the fluid density. Following tradition,

quantities normalized with inner (or viscous) units, i.e. with the friction velocity and the viscous length $\delta_\nu = \nu/U_*$, will be indicated with the superscript $+$. The standard setting used for the DNS of turbulent channel flows between two planar, parallel walls is used in the present simulations, with periodic boundary conditions assigned to the velocity in the two wall-parallel directions of the computational domain and with an enforced constant mass flux through the channel.

Under the conditions stated above, the non-dimensional equations for the Lagrangian evolution of particle positions and velocities read

$$\frac{\mathrm{d}\boldsymbol{v}^p}{\mathrm{d}t} = \frac{\boldsymbol{u}(\boldsymbol{x}^p(t), t) - \boldsymbol{v}^p}{St}, \tag{2.3}$$

$$\frac{\mathrm{d}\boldsymbol{x}^p}{\mathrm{d}t} = \boldsymbol{v}^p, \tag{2.4}$$

where $\boldsymbol{v}^p$ and $\boldsymbol{x}^p$ denote the velocity and position of the pth particle, respectively. The Stokes number St is defined as the ratio between the particle response time $\tau_p = \rho_p d_p^2/(18\rho\nu)$, with d_p the particle diameter and ρ_p its density, and an integral time scale h/U_c. In this context, the only parameter controlling the particle dynamics for a given flow field is the Stokes number. The natural choice for a characteristic time scale in wall-bounded turbulent flows is the viscous time scale ν/U_*^2. Accordingly, the viscous Stokes number is defined as $St^+ = \tau_p U_*^2/\nu$. An initially uniform distribution of particles is introduced in the computational domain and allowed to evolve in interaction with fully developed turbulence up to attaining the statistical steady state. In the present context, this amounts to assuming, also for the particles, periodic boundary conditions in the streamwise and spanwise directions, i.e. when a particle reaches the artificial boundary of the computational domain, it is reintroduced from the opposite side. The interactions with the solid walls of the channel are treated as purely elastic rebounds, occurring when the distance between particle centre and wall equals the particle nominal radius. There are many factors influencing the particle–wall interaction, such as roughness, particle and wall elasticity, chemical electrostatic interactions, hydrodynamical lubrication forces and many more. These effects are usually condensed using a global parameter, the *restitution coefficient* $e = |u_2/u_1|$, where u_1 and u_2 are the wall-normal component of the particle velocity before and after the collision against the wall. A unit value indicates pure elastic rebound, while a zero value implies particles that stick to the wall. The effect of inelastic collisions with $e = 0.9$ on turbophoresis is addressed in the paper of Li *et al.* (2001), showing negligible differences in the results between simulations with pure elastic rebound ($e = 1$) and with inelastic ones ($e = 0.9$). For the above reasons, only cases with ideal elastic collisions are simulated in the present work.

The DNS data in the channel-flow geometry were obtained with an adapted version of the spectral Navier–Stokes solver SIMSON (Chevalier *et al.* 2007). For the fluid phase, streamwise and spanwise directions are discretized with Fourier series, whereas the wall-normal direction is expanded in Chebyshev polynomials, with no-slip and impermeability boundary conditions at the two walls enforced by the so-called tau method (Canuto *et al.* 1988). The position of the grid points in the wall-normal direction follows the Gauss–Lobatto distribution, providing fine resolution in the layer adjacent to the wall. A low-storage four-stage mixed Runge–Kutta/Crank–Nicolson scheme is employed for temporal discretization. The nonlinear terms are evaluated in physical space by means of fast Fourier transform (FFT) employing the so-called 3/2 rule de-aliasing procedure in the wall-parallel directions. The code has been successfully validated for single-phase turbulent channel flow at various Reynolds

numbers up to $Re_\tau = 590$, and gives essentially the same results as those in Moser, Kim & Mansour (1999); therefore it is not further discussed. In order to run efficiently on massive parallel cluster computers, an MPI (message passing interface) parallelization over the spanwise direction has been used for the present simulations.

The numerical integration of positions and velocities of the Lagrangian particles is achieved by the same Runge–Kutta scheme as used for the carrier phase. The fluid velocities at the particle locations are interpolated by a trilinear scheme able to provide the required accuracy everywhere in the field, especially in the near-wall region, where the grid becomes finer (Sardina *et al.* 2011). We remark that a similar interpolation formula was successfully exploited in the pseudo-spectral DNS of the homogeneous shear flow (Gualtieri *et al.* 2009). The particle-tracking algorithm is parallelized using MPI as well, thus enabling the treatment of large domains employing of the order of 100 processors.

The implementation of this mixed Eulerian–Lagrangian algorithm has been validated by comparing, at matching parameters, the results of the simulation at $Re_\tau = 150$ with those provided in the database by Marchioli *et al.* (2008) for three different particle populations with Stokes numbers $St^+ = 1$, 10 and 25. The mean streamwise particle velocity and its fluctuations are shown in figure 1 by solid lines, where the particles with $St^+ = 1$ most closely reproduce the mean fluid velocity. These data correspond almost exactly to those of Kuerten (symbols) contained in the cited database, with turbulence intensities and Reynolds stresses sharing peak values and relative positions.

The main data set to be addressed in the present paper consists of two channel-flow simulations at a slightly larger Reynolds number, $Re_\tau = 180$, maintained by a fixed mass flux, which are identical except for the dimensions of the computational domain. The size of the smaller domain is $4\pi \times 2 \times 4\pi/3$, matching the benchmark simulation of Moser *et al.* (1999), discretized with a total of $128 \times 129 \times 128$ spectral modes. This simulation will be denoted by the letter S in the following. These are the typical domain dimensions used in most of the published literature on turbulent particle-laden channel flows. In recent times, however, it has become clearer that a small computational domain may induce a substantial phase locking on the largest turbulent structures (see e.g. del Álamo & Jiménez 2003). We speculate that the resulting blockage effect has an impact also on the dynamics of the dispersed phase, an issue that deserves a deeper investigation. To demonstrate the consequences of an insufficient box size, we consider a substantially larger domain with size $12\pi \times 2 \times 4\pi$, matching the dimensions of the simulation in del Álamo & Jiménez (2003). Accordingly, the number of grid points in the larger simulation is increased by a factor of 3 in both the wall-parallel directions, i.e. $384 \times 129 \times 384$ grid points. This simulation will be denoted L in the following. A comparison between the two domains is sketched in figure 2.

A total of six particle populations is considered, differing only in the Stokes number ($St^+ = 0$, 1, 5, 10, 50, 100). The different Stokes numbers are obtained by changing the radius of the particle populations (see table 1) at fixed density ratio between the two phases, $\rho_p/\rho = 770$. The two simulations evolve 200 000 and 1 800 000 particles per population, in order to keep the same average spatial concentration. Each simulation was started from a fully developed turbulent velocity field obtained in the respective boxes seeded with random, homogeneously distributed particles. Each simulation was kept running for long enough (final time $t_{fin}^+ = 30\,000$) to reach and accurately sample the eventual statistical steady state of the particle distributions. After reaching this steady state, in the time interval $t^+ = 10\,000$ to $30\,000$, ~ 100 time-independent fluid velocity fields with corresponding particle configurations and
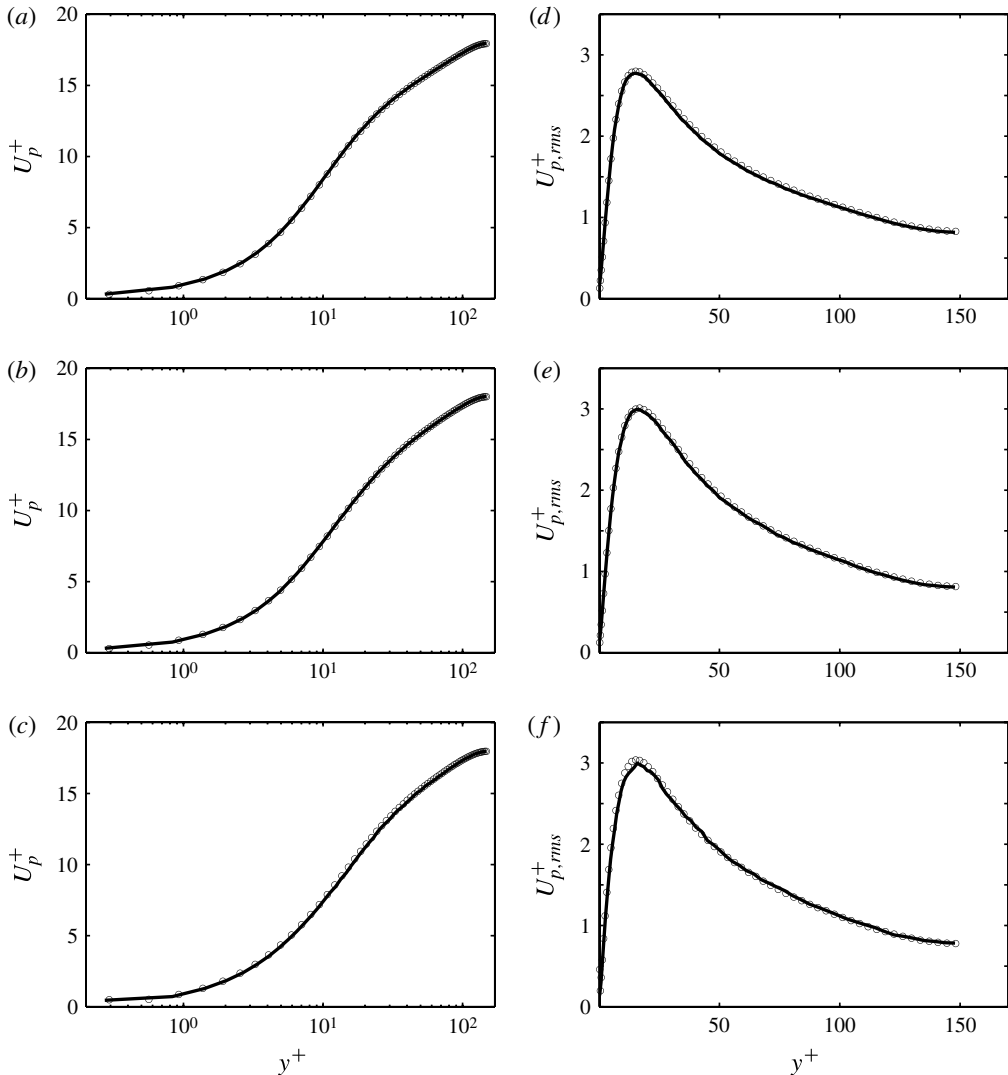
FIGURE 1. (a–c) Mean streamwise particle velocity U_p^+ in the channel-flow simulation at $Re_\tau = 150$. (d–f) Root mean square streamwise particle velocity fluctuations $U_{p,rms}^+$. The particle populations are ordered from the top down according to their inertia: (a,d) $St^+ = 1$; (b,e) $St^+ = 5$; (c,f) $St^+ = 25$. The solid lines represent our simulation, while the circles correspond to the data of Kuerten's DNS described in Marchioli *et al.* (2008).

St^+	0	1	5	10	50	100
r^+	—	0.076	0.17	0.24	0.54	0.76

TABLE 1. Particle population parameters: viscous Stokes number St^+ and radius in viscous units $r_p^+ = d_p^+/2$. Density ratio $\rho_p/\rho = 770$.
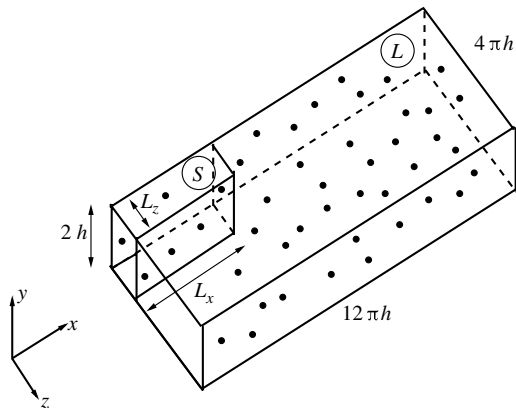
FIGURE 2. Sketch of the simulation domains with the employed coordinate systems. *S* denotes the smaller domain and *L* the larger one.

velocities were collected for statistical analysis. We stress that domain dimensions and particle number of the larger simulation are presumably the largest ever used so far for multiphase wall-bounded flows This simulation required ∼200 000 core hours on a Linux cluster, running on 128 cores in parallel.

3. Results

3.1. *Instantaneous snapshots*

Figure 3 shows, for the larger simulation, an instantaneous particle configuration (light dots) in a wall-parallel plane close to one of the two solid walls bounding the channel. As is well known, turbulence induces a drift towards the wall and leads to the eventual accumulation of the particles in the wall region (see e.g. Reeks 1983). As apparent from the figure, the particles are unevenly distributed, with larger local density occurring in elongated clusters. From visual inspection, the clusters are extremely long and persistent. Their substantial streamwise extension actually casts doubt on the reliability of simulations performed in smaller domains, where a single particle cluster may easily run from side to side across the entire computational box.

We stress here that our larger domain is selected to have negligibly small fluid velocity correlation between points separated in the streamwise and spanwise directions by half the corresponding domain length, e.g. for the streamwise velocity fluctuation $u'(x, y, z, t)$,

$$\langle u'(x, y, z)u'(x + L_x/2, y, z)\rangle \ll 1, \quad \langle u'(x, y, z)u'(x, y, z + L_z/2)\rangle \ll 1, \quad (3.1)$$

where angular brackets imply both spatial averaging in the two wall-parallel directions and ensemble averaging with respect to the two channel halves and the set of independent fields collected at the statistical steady state.

The contours shown in the background of the image provide the iso-levels of the streamwise fluctuation velocity of the carrier fluid, showing the well-known streaky structures with alternating regions of local velocity excess (lighter tones) and defect (darker tones) (Kline *et al.* 1967). This single, generic image already highlights a strong correlation between particle positions and streamwise fluid velocity. It is immediately clear that particles are preferentially located in regions with instantaneous streamwise fluid momentum deficit, the so-called low-speed streaks. These results are
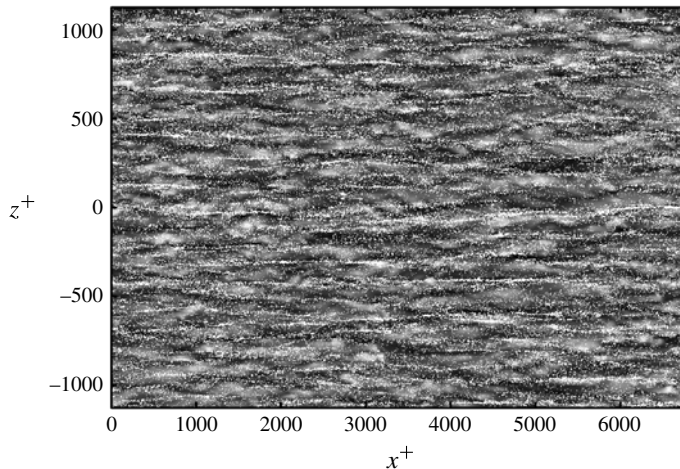
FIGURE 3. Snapshot of the particle distribution ($St^+ = 10$) in the viscous region $y^+ < 5$ at $t^+ \simeq 25\,000$. The background contour represents the velocity field, darker regions indicating low-speed fluid. The plot shows the whole extent of the large domain (not to scale), simulation L.
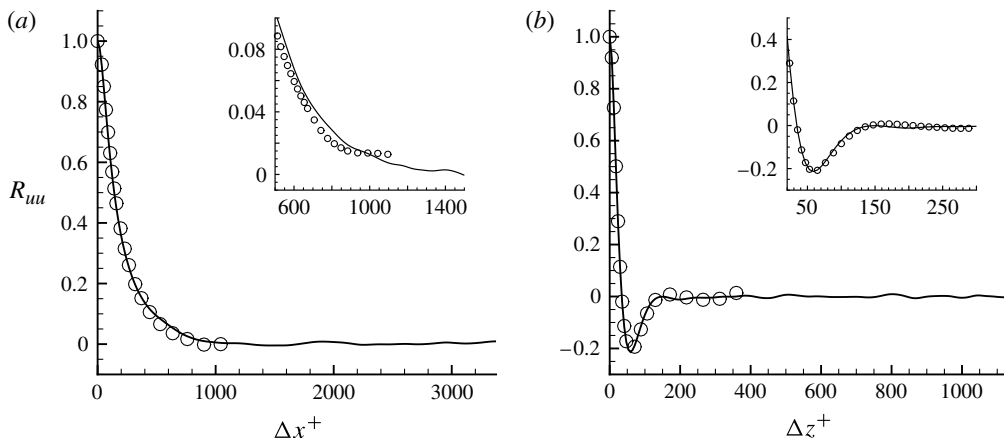
FIGURE 4. (*a*) Streamwise and (*b*) spanwise longitudinal velocity correlations for the large-domain L (solid line) and the small-domain S (circles) simulations at $y^+ = 15$. Enlargements are provided in the two insets.

in good agreement with a number of previous observations (see Rouson & Eaton 2001; Picciotto *et al.* 2005; Picano *et al.* 2009, among others), where particles were found to persist in regions of low fluid velocity.

As shown in figure 4, the smaller domain S is not long enough to allow decorrelation of the velocity signal, violating condition (3.1). The resulting phase locking of the fluid velocity streaks is expected to affect the distribution of particles in the small domain. The issue is qualitatively addressed in figure 5(*a*), which provides a comparison between two generic instantaneous particle configurations taken from the two simulations, one in the small and the other in the large computational box. The
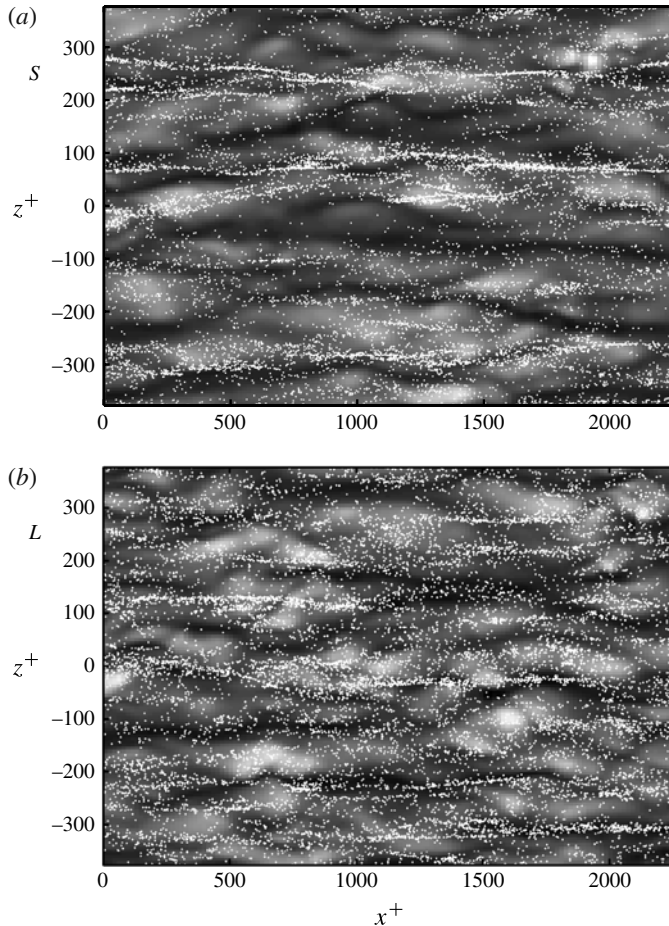
FIGURE 5. Instantaneous snapshots of the particle distribution ($St^+ = 10$) in the viscous region at $t^+ \simeq 25\,000$. Particles are shown as light dots superimposed onto the contours representing the streamwise velocity component (dark represents low-speed fluid). (*a*) Entire flow domain of the small simulation *S*. (*b*) Corresponding part of the large-domain simulation *L*; see figure 3 for a view of the whole domain. Plots are not drawn to scale.

shown wall-parallel slice spans the entire streamwise and spanwise extent of the small domain. Figure 5(*b*) displays on the same scale the corresponding portion of the larger domain; see figure 3 for the complete view. The effect of the computational box size on the gross features of the particle distribution is apparent. Although the average particle number per unit volume is identical in the two cases, the image of the small domain shows a substantially lower local concentration. This suggests that one of the artifacts of the improper dynamics of the largest fluid velocity structures is a decrease in the effectiveness of turbophoresis, significantly underestimated in the presence of artificial confinement. A second artifact is the increased order of the individual particle aggregates, which look much straighter in the streamwise direction, and more regularly spaced in the spanwise direction. Both observations are clear indications that the collective dynamics of the particles is altered, since, as discussed in more detail in Picano *et al.* (2009), preferential localization is the essential mechanism

leading to statistical equilibrium. Actually, in wall turbulence, particles are always subject to turbophoretic drift, which is responsible for pumping the particles from the bulk towards the walls, thus establishing the particle number density gradient corresponding to the eventual accumulation at the wall. At steady state, the particles need to oversample fluid motions departing from the wall region to balance the turbophoretic drift (Reeks 1983; Young & Leeming 1997; Picano *et al.* 2009). This is achieved by a correlation of particle positions and fluid velocity events directed from the wall towards the bulk of the channel (Rouson & Eaton 2001; Picciotto *et al.* 2005), which requires particle persistence in the low-speed streaks. The enhancement of near-wall concentration is the outcome of such a delicate balance between particles that leave the wall region in exchange for an opposite flux due to turbophoresis.

3.2. *Analysis of wall accumulation*

In order to make our analysis more quantitative, we need a global indicator able to distinguish between different particle distributions in terms of the amount of wall accumulation. The concept of Shannon entropy can serve for this. This quantity, borrowed from statistical mechanics and information theory, was introduced by Picano *et al.* (2009) as a global measure of particle segregation in turbulent wall-bounded flows. For the present cases, the whole computational domain is divided into $N_{sd} = 128$ equidistant wall-parallel slabs with dimensions $L_x \times 2h/N_{sd} \times L_z$ and height $h_{sd}^+ = U^*(2h/N_{sd})\nu = 2\,Re_\tau/N_{sd} = 2.8$. The probability of finding a particle in subdomain i is $p_i = N_i/N_t$, where N_i is the average number of particles in subdomain i, with N_t the total number of particles. The coarse-grained probability distribution p_i, $i = 1, \ldots N_{sd}$, describes how particles are distributed as a function of distance from the wall. An entropy, defined as $\mathscr{S} = -\sum_i^{N_{sd}} p_i \ln p_i$, can be conveniently attached to this coarse-grained probability distribution. The entropy varies between zero, corresponding to all the particles being located within the same subdomain, to a maximum, $\mathscr{S}_{max} = \ln N_{sd}$, which is achieved with uniform distribution, $p_i = 1/N_{sd}$. By normalizing the entropy with its maximum, we construct an indicator, the normalized entropy, $S = \mathscr{S}/\mathscr{S}_{max}$, which ranges from 0, when all particles are located in the same subdomain, to 1, when the particles are equally distributed among the domains.

Figure 6 provides the time evolution of the entropy $\mathscr{S}$ for the two simulations in the small and large domains, for each particle population. All curves start from unity, since the particle initial positions were assigned with uniform spatial distribution. The entropy decreases while the particles continue to localize more and more in the subdomains closest to the walls. All populations reach a steady-state distribution, with the only exception being particles at $St^+ = 5$ whose entropy is still decreasing at the time the simulation is stopped. The lightest particles ($St^+ = 1$) essentially behave as Lagrangian tracers and keep the uniform distribution they had initially. The smallest asymptotic entropy, corresponding to largest accumulation, is achieved by particles with Stokes numbers in the range $St^+ = 10$–50. For such particles, the Stokes number based on the local time scale of the buffer layer is of order one, confirming the accepted explanation that takes the coherent structures of the buffer layer as the engine of turbophoresis. On the contrary, particles with $St^+ = 100$ show a higher asymptotic entropy value corresponding to a lower wall accumulation.

Furthermore, figure 6 quantitatively confirms the qualitative differences in the particle distributions between the large and small domains discussed in connection with figure 5. Although the transient phase is qualitatively similar between the two boxes, the particles get much more segregated in the large domain. Apparently, the delicate balance between turbophoretic drift and preferential sampling of fluid velocity
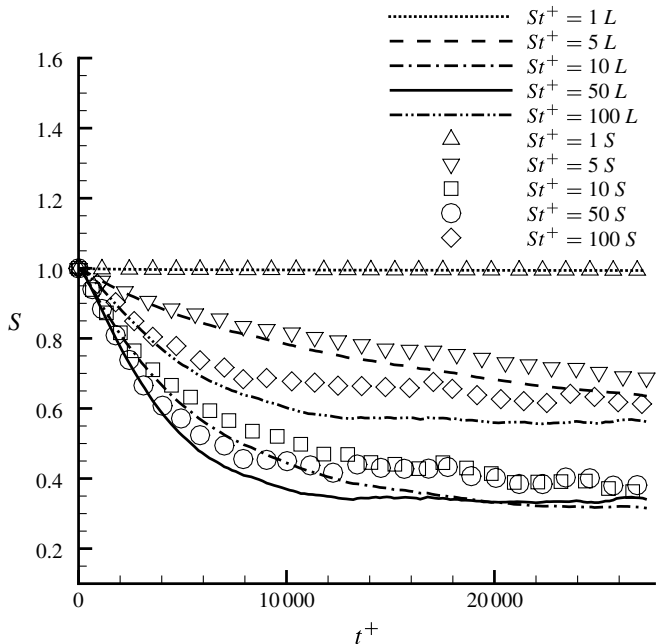
FIGURE 6. Shannon entropy of the mean particle distribution versus viscous time t^+ for each particle population in the large domain L (lines) and the small domain S (symbols).

events directed away from the wall is extremely sensitive to the large-scale fluid motions, inhibited in the small domain as a result of the imposed periodicity of the flow.

As a global feature of the distribution, the Shannon entropy does not give information concerning the specific regions where particles accumulate. This detail is immediately spotted in figure 7(*a*), showing in logarithmic scale the wall-normal profiles of the normalized mean particle concentration $c(y)$, defined as the ratio of particle number per unit volume to bulk concentration (ratio of total particle number to whole domain volume). The large particle accumulation near the wall stands out. While Lagrangian tracers are uniformly distributed at all times, inertial particles manifest a concentration maximum close to the wall whose intensity strongly depends on their inertia. The concentration peaks are found to move outwards slightly with increasing Stokes number. This behaviour is essentially due to the finite distance at which particle–wall collisions take places, i.e. the particle radius. Since different particle populations are obtained on changing the particle radius (see table 1), the minimum possible distance from the wall increases with the Stokes number. As anticipated, the highest wall concentrations are exhibited by particles with $St^+ = 10, 50$, whose local wall density reaches of the order of a thousand times the values in the centre of the channel. Actually, the largest particles, $St^+ = 100$, show a higher concentration than particles with $St^+ = 10, 50$ in the range $2 < y^+ < 10$, but with a lower concentration peak near the wall.

The difference between the large and small domains in terms of particle concentration is highlighted in figure 7(*b*), where the ratio of large- to small-domain concentration is plotted as a function of wall-normal distance. The difference is significant (of the order of 20 %) and the particles apparently accumulate at the wall
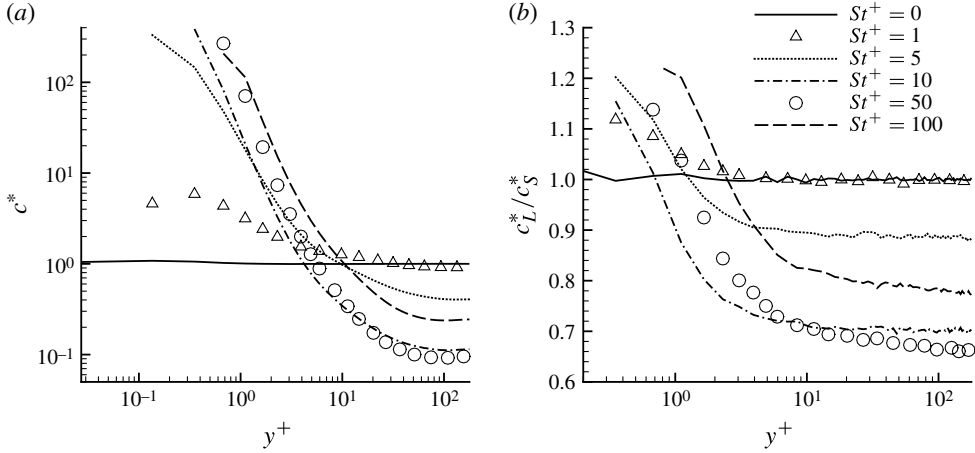
FIGURE 7. (*a*) Steady-state mean normalized particle concentration for the large-domain simulation *L*. (*b*) Ratio between concentrations in the large and the small domains.

much more in the larger box even for particles at $St^+ = 1$. The largest difference is achieved by particles with $St^+ = 100$. These massive particles are mostly driven by the low-frequency fluid motions. Hence this behaviour is attributed to the difference in the large-scale turbulent structures induced by the confinement due to periodic boundary in the two configurations.

3.3. *Particle velocity probability density function*

As already stated, the equilibrium wall concentration is controlled by the ability of the particles to oversample departing fluid events in order to balance the turbophoretic drift. To quantify the concept, preferential sampling of fluid velocity events can be addressed by looking at the difference between average fluid velocity at a particle position, i.e. the average fluid velocity sampled by particles $\langle u|_p \rangle$, and unconditioned average fluid velocity $\langle u \rangle$.

Figure 8(*a*) shows the p.d.f. of the wall-normal particle velocity during the steady state in the buffer layer $(5 \leqslant y^+ \leqslant 30)$. In describing the results, the wall-normal velocity is assumed positive when directed towards the wall, i.e. different from the usual convention. The thick solid line is the p.d.f. of fluid velocity. This statistic is essentially identical in the large and the small domains, indicating the good agreement for the fluid. The other lines in figure 8 provide the p.d.f.s of the wall-normal particle velocity in the large domain, with symbols indicating small-domain data. We see that even the single-point particle velocity p.d.f. seems to be unaffected by domain truncation. We further remark that the mean value of the particle wall-normal velocity is zero because the statistical steady state is considered. The larger is the inertia, the less frequent are the intense particle velocity events, i.e. the tails of the p.d.f., compared with the fluid ones. This effect is more accentuated for intense departing events (negative tail). On the contrary, slow motions directed away from the wall are more frequent compared to fluid, as can be seen from the insets. Hence the particles move mainly with slow departing velocities and tend to filter out high-velocity fluctuations, especially those directed away from the wall and towards the channel centre. This trend is shared by all populations and is more evident for the largest particles.
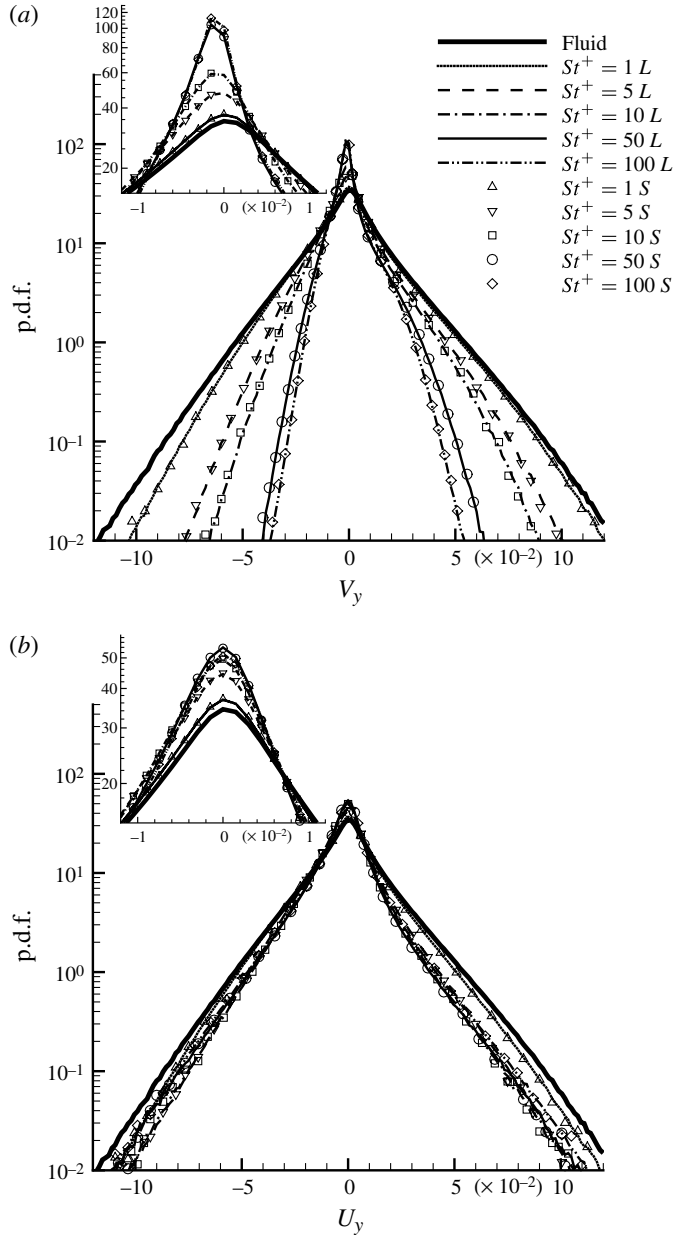
FIGURE 8. The p.d.f.s of (*a*) wall-normal particle velocity and (*b*) wall-normal fluid velocity sampled by particles in the buffer layer ($5 \leqslant y^+ \leqslant 30$) at statistically steady state. Enlargements are provided in the insets. Positive wall-normal velocities are directed towards the wall.

Since the particles are not uniformly distributed in space, this implies that they can sample specific fluid events. The p.d.f. of wall-normal fluid velocity conditioned to the particle positions, i.e. the fluid velocity 'seen' by the particles, is used to quantify the preferential sampling – see Picano *et al.* (2009) for more details. This p.d.f. gives
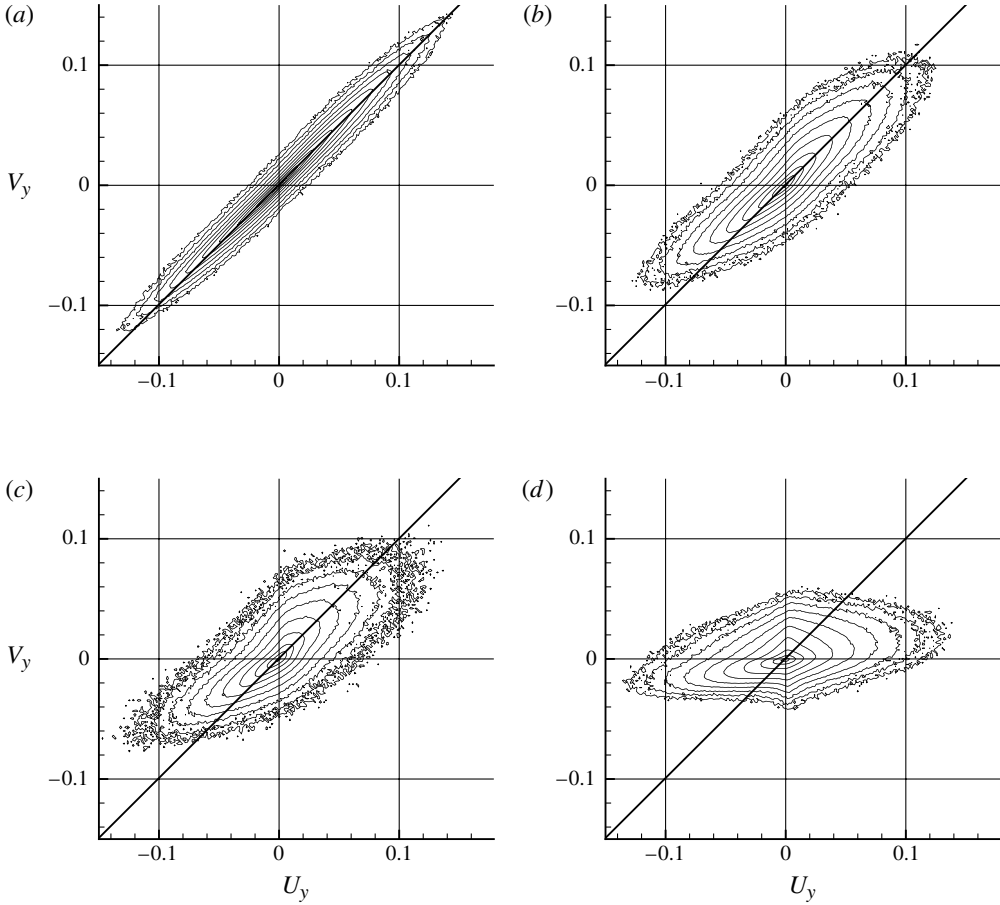
FIGURE 9. Joint p.d.f. of wall-normal particle velocity V_y and particle-sampled fluid velocity U_y in the buffer layer for four different Stokes number in the large-domain simulation: (*a*) $St^+ = 1$, (*b*) $St^+ = 5$, (*c*) $St^+ = 10$ and (*d*) $St^+ = 100$. Positive velocities are directed towards the wall.

the normalized number of particles that are subject to a certain fluid velocity event. Hence, comparing the fluid velocity p.d.f. seen by the particles with the unconditioned one, it is possible to assess in which regions the particles preferentially localize. From figure 8(*b*), inertial particles tend to undersample the intense fluid events (p.d.f. tails) and especially those directed towards the wall (positive values). Conversely, the particles tend to oversample slow fluid motions and particularly those away from the wall (ejection motions). This feature is more accentuated for particles with $St^+ = 50$. It is expected that the maximum preferential sampling occurs for intermediate Stokes numbers, since tracers ($St^+ \to 0$) and ballistic particles ($St^+ \to \infty$) sample the fluid events uniformly. The particle preferential sampling of slow departing motions is consistent with the localization in streaky patterns corresponding to the low-speed streaks, as discussed with regard to figure 5.

More details can be extracted from the joint probability distribution function (JPDF) of particle and fluid velocity. The JPDF is shown in figure 9 for the buffer layer where most of the turbophoresis originates. The lightest particles $St^+ = 1$ (figure 9*a*) tend
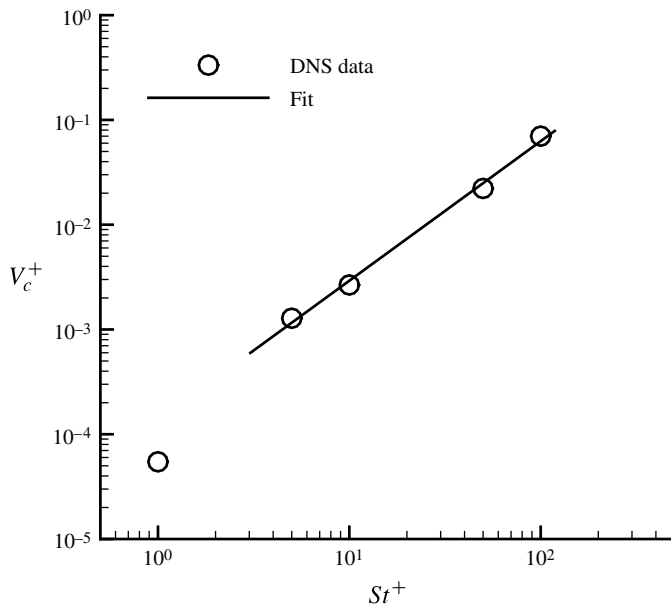
FIGURE 10. Average collision velocity at the wall V_c^+ versus Stokes number St^+ (log scale): circles, DNS data; full line, fit $V_c^+ \propto (St^+)^{1.33}$.

to reproduce the fluid velocity accurately, as shown by the bottom-left to top-right alignment of the JPDF iso-levels, which imply that $V_y \simeq U_y$, with the exception of the negative tail (intense departures from the wall), where particles are strictly slower than the fluid. In this third quadrant, the particle speed is systematically smaller than the corresponding fluid velocity, suggesting that even low-inertia particles cannot fully comply with abrupt fluid departures from the wall. A similar but more accentuated trend is apparent for particles with $St^+ = 5$, 10 (figure 9*b,c*). As a general feature, particles follow the fluid, approaching the wall in quasi-symmetrical fashion, with almost equiprobable positive and negative relative velocity with respect to the fluid. On the other hand, they move systematically more slowly than the fluid in departing motions. On increasing the Stokes number, ballistic behaviour is eventually achieved, and at $St^+ = 100$ (figure 9*d*) particle velocities are much less correlated with the fluid. The small amount of accumulation experienced by these heavy particles may be understood by the fact that they do not even follow the fluid in the approaching motions. The rhomboidal shape of the JPDF contours is induced by the collisions with the wall, which are very intense owing to the large inertia. Note that, the larger the inertia, the higher the wall collision velocity and the longer the spatial distance where particles maintain a given velocity. A measure of this effect can be given by the average collision velocity at the wall, V_c^+, as a function of St^+ (see figure 10). As can be seen in the figure, the collision velocity increases with the Stokes number, and for $St^+ \geqslant 5$ the data are well fitted by the power law $V_c^+ \propto (St^+)^{1.33}$. Since a particle tends to maintain its velocity for a time scale of the order of its particle relaxation time τ_p, the length l_{col}, where the effect of the wall collision is relevant, is $l_{col}^+ = l_{col}/(\nu/U_*) = V_c^+ St^+$. The estimate of l_{col}^+ for particles with $St^+ = 100$ is $l_{col}^+ \simeq 7$, while for particles with $St^+ = 10$ it is $l_{col}^+ \simeq 0.03$. This explains why the ballistic behaviour in the buffer layer is apparent only for our largest particles, $St^+ = 100$.
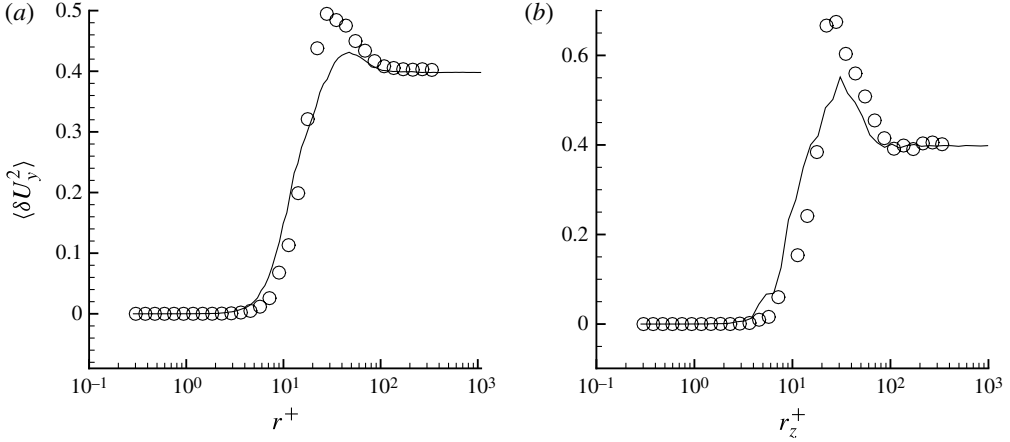
FIGURE 11. Second-order structure function of wall-normal fluid velocity in the buffer layer at $y^+ = 15$ for the two domains (full line, large domain; circles, small domain): (*a*) angular average, $\langle \delta U_y^2 \rangle_0$ (see (3.3)) versus separation r^+; and (*b*) spanwise cut, $\langle \delta U_y^2 \rangle (r_x^+ = 0, r_z^+)$ (see (3.2)) versus spanwise distance r_z^+.

The bias in the departing events discussed in connection with the particle velocity p.d.f. (figure 8*a*) is entirely consistent with the behaviour of the JPDF (figure 9) in the third quadrant. At a qualitative level, it is explained by the particle inertia filtering out the strong acceleration associated with the most intense outburst of fluid. Unexpectedly, no relevant difference seems to emerge in the single-point velocity statistics between the two simulations *L* and *S*, in the large and small domains, respectively.

3.4. *Two-point statistical analysis*

Proceeding to higher-order statistics, figure 11 addresses the wall-normal fluid velocity differences in terms of the second-order wall-normal structure function,

$$\langle \delta U_y^2 \rangle = \langle (U_y(x + r_x, y, z + r_z) - U_y(x, y, z))^2 \rangle, \tag{3.2}$$

which, for given wall-normal position, depends on the separation vector $\boldsymbol{r} = (r_x, r_z) = r(\cos\theta, \sin\theta)$. Figure 11(*a*) shows the angular average

$$\langle \delta U_y^2 \rangle_0 = \frac{1}{2\pi} \int_0^{2\pi} \langle (U_y(x + r\cos\theta, y, z + r\sin\theta) - U_y(x, y, z))^2 \rangle \, d\theta, \tag{3.3}$$

while figure 11(*b*) gives the spanwise behaviour for $r_x = 0$. The spanwise structure function neatly defines the transverse correlation scale of the wall-normal fluid velocity. Comparing data in the large domain *L* (solid line) and the small domain *S* (symbols), the alteration of the peak intensity clearly appears, confirming the blockage induced by insufficient domain dimensions. Specifically, the more coherent and aligned structures found in the small domain here appear as an enhanced peak at the correlation scale. We clearly expect a similar effect on the two-point particle statistics.

Particle clustering is best addressed in terms of two-point statistics of particle positions. Given an instantaneous configuration of particles, clustering amounts to an increased probability of finding a second particle in the neighbourhood of a first one with respect to a reference distribution where particles are randomly distributed in

space. This effect is typically studied by analysing the radial distribution function, which provides the probability of finding a particle pair separated by a given separation r. This tool has been used and thoroughly discussed for homogeneous flows by Bec *et al.* (2007), Shotorban & Balachandar (2006) and Gualtieri *et al.* (2009), among others.

In the present case, clustering occurs in combination with turbophoresis, spatial inhomogeneity and strong anisotropy. The appropriate statistical observable is the ADF (e.g. Gualtieri *et al.* 2009), which is the direct extension of the RDF to take into account the angular dependence. This concept can be specialized to deal with the geometry of wall-bounded flows, where the interest is focused on the directionality of particle distributions in wall-parallel planes at given wall-normal distance y. For this purpose, it is useful to introduce a two-dimensional version of the ADF,

$$g(r, \hat{\boldsymbol{r}}, y) = \frac{1}{r} \frac{\mathrm{d}\nu_r}{\mathrm{d}r} \frac{1}{n_0(y)}, \qquad (3.4)$$

where $\nu_r(r, \hat{\boldsymbol{r}}, y)$ is the average number of pairs in the same plane within distance r along the wall-parallel direction, represented by unit vector $\hat{\boldsymbol{r}}$, and

$$n_0(y) = 0.5 N_p(y)[N_p(y) - 1]/(L_x L_z) \qquad (3.5)$$

is the total number of pairs in the plane divided by the area of the system. Given its normalization, the ADF does not depend on the mean concentration of the specific plane and is related to the probability of finding a particle pair normalized by the probability of a random, spatially decorrelated particle arrangement. Hence, for spatially homogeneous, independent distributions of particle positions, the ADF would be identically equal to 1 in all planes, for all distances and directions. The actual number of particle pairs $\mathcal{N}(\xi, y)$ expected in a small circular domain of radius $\xi \ll 1$, say, is expressed in terms of the ADF as

$$\mathcal{N}(\xi, y) = n_0(y) \int_0^{2\pi} \int_0^{\xi} r g(r, \hat{\boldsymbol{r}}, y) \, \mathrm{d}r \, \mathrm{d}\theta, \qquad (3.6)$$

where the unit vector $\hat{\boldsymbol{r}}$ lies in the wall-parallel plane at wall-normal position y and θ is the angle defining its direction in the plane. For spatially independent particle positions, the number of pairs is $\mathcal{N}(\xi, y) = n_0(y)\pi\xi^2$, corresponding to bounded ADFs for vanishing separations. In the presence of clustering, the probability of finding a second particle in the vicinity of a given one is instead much increased. Hence, when small-scale clustering ($\xi \ll 1$) occurs, $\mathcal{N}(\xi, y) > n_0(y)\pi\xi^2$, implying that $g(r, \hat{\boldsymbol{r}}, y) \propto r^{-\alpha}$, with $\alpha > 0$ for small r (Sundaram & Collins 1997; Bec *et al.* 2007). The singularity exponent α can thus be taken as a measure of the small-scale clustering intensity.

Before discussing the results in more depth, it may be worth stressing once more that preferential accumulation at the wall and clustering, although strictly entangled in wall flows, are two distinct phenomena. In principle, preferential accumulation at the wall could also occur with no relevant clustering effects, like in a laminar stratification process. Under these conditions, the ADF would be identically unity everywhere, while the mean concentration could have a wall-normal variation. Conversely, clustering can take place without turbophoresis in homogeneous particle-laden turbulent flows. In wall-bounded flows, as we will show, the two phenomenologies are complementary aspects of the same physics.

In figure 12 the ADF is plotted as a function of $r_x = r\hat{r}_x$ and $r_z = r\hat{r}_z$ in the viscous sublayer (figure 12a–d) and in the outer region (figure 12e–h) for the large-domain
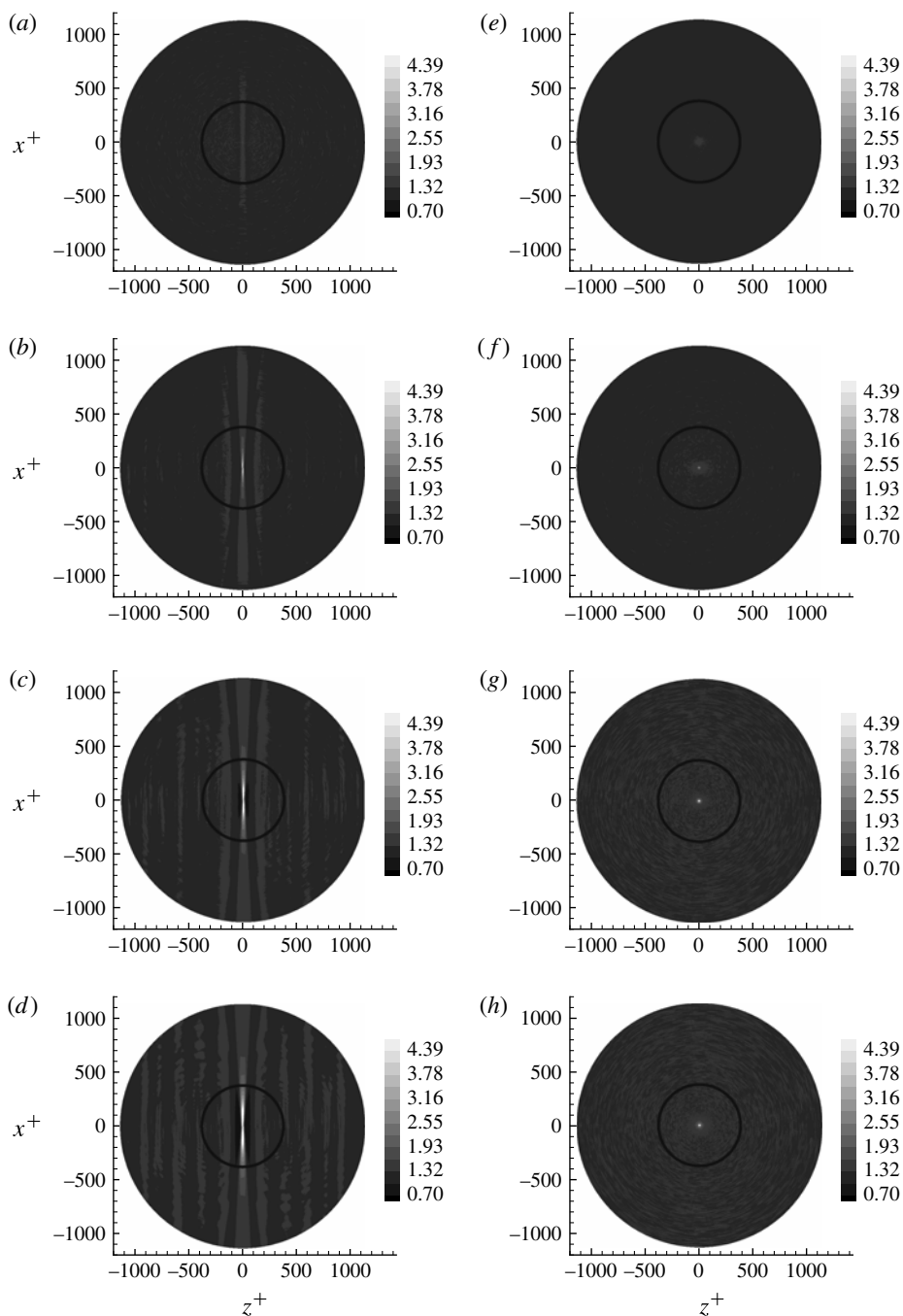
FIGURE 12. ADF for four different Stokes numbers, $(a$–$d)$ in the viscous sublayer $y^+ = 3$ and $(e$–$h)$ in the outer region $y/h = 1$ for the large-domain simulation: (a,e) $St^+ = 1$; (b,f) $St^+ = 5$; (c,g) $St^+ = 10$; and (d,h) $St^+ = 50$. The circle indicates the limit of the small domain.

simulation and different Stokes numbers. As already explained, the increase near the origin, $r \to 0$, is a manifestation of small-scale clustering. Actually, this is the most relevant feature characterizing the outer region (figure 12*e–h*), especially for particles with Stokes number $St^+ = 10$, 50. The circular symmetry of the ADF in this region implies the absence of a preferred direction in the wall-parallel plane, as expected, for example, for isotropic particle aggregates. In fact, small-scale clustering is a persistent feature of the system, found also in the near-wall region. However, the directionality of the clusters, negligible further away from the wall, becomes more and more apparent as the wall is approached and becomes overwhelmingly strong in the viscous sublayer. In the streamwise direction $\hat{\boldsymbol{e}}_x$, the ADF, $g_x(r) = g(r, \hat{\boldsymbol{e}}_x)$, systematically exceeds unity, showing that, independently of separation, the number of particle pairs in the streamwise direction is, for any distance, larger than expected on the basis of a spatially independent distribution ($g \equiv 1$). Geometrically, $g_x(r) = g(r, \hat{r}_x) > 1$ corresponds to the preferential streamwise alignment of the particle streaks. On the contrary, in the spanwise direction, $\hat{\boldsymbol{e}}_z$, the ADF, $g_z(r) = g(r, \hat{\boldsymbol{e}}_z)$, falls below unity to reach a minimum at $r = l_c$. This is interpreted as a smaller probability of finding particle pairs in that direction at the corresponding separation. This happens at a typical distance that defines the thickness of the particle streak, when one particle is within the high-density region and the other in the depleted area that separates neighbouring streaks. This anisotropic behaviour is particularly relevant for intermediate size particles, i.e. $St^+ = 10$, 50.

The diameter of the black circles included in each plot in figure 12 corresponds to the spanwise extent of the small domain. It is clear that, in the near-wall region, the spanwise scale of the small domain is insufficient to fully resolve the near-wall particle clustering.

Cuts of the ADF along the streamwise direction $\hat{\boldsymbol{e}}_x$ are plotted in figure 13 for different Stokes numbers in order to highlight the length scales of the clusters. In the streamwise direction, particle positions remain highly correlated up to separations of the order of 500–1000 wall units, a correlation length physically induced by the fluid velocity structures. Such a correlation length should be compared with the streamwise extension of the large ($L_x^* = 12\pi \times 180 \simeq 6800$) and the small ($L_x^* = 4\pi \times 180 \simeq 2300$) domains. While $g_x \equiv 1$ at large distance in the large domain, with the exception of particles with Stokes number $St^+ = 1$ (not reported in figure), the small domain is too short for the correlation between particles positions to properly vanish. As a consequence of confinement, for Stokes numbers 5–10, the probability of finding a pair along the streamwise direction at the largest scales in the short domain is significantly larger in the short than it is in the long domain, denoting an even increased particle correlation. This alteration extends to smaller scales as the particle inertia increases, $St^+ = 50$–100, as shown by the ADF of the short domain, which, for heavy particles, almost everywhere exceeds that of the longer domain. Overall the analysis of the ADFs confirms the qualitative impression already given by figure 5: in the small-domain simulation the particle distributions are systematically more aligned in the streamwise directions.

Figure 14 shows the behaviour of the ADF in the spanwise direction. The streaky nature of the particle patterns emerges clearly from this observable. The characteristic spacing of the particle streaks corresponds to twice the spanwise separation l_c where the ADF minimum occurs. This spanwise length is found to be around $l_c^+ \simeq 30$ wall units for $St^+ = 5$, 10, 50 in the large domain and $l_c^+ \simeq 40$ wall units in the small one. It is clearly related to the spanwise correlation length of wall-normal fluid velocity fluctuations ℓ_z. For particles with $St^+ = 100$, the spanwise scale increases to
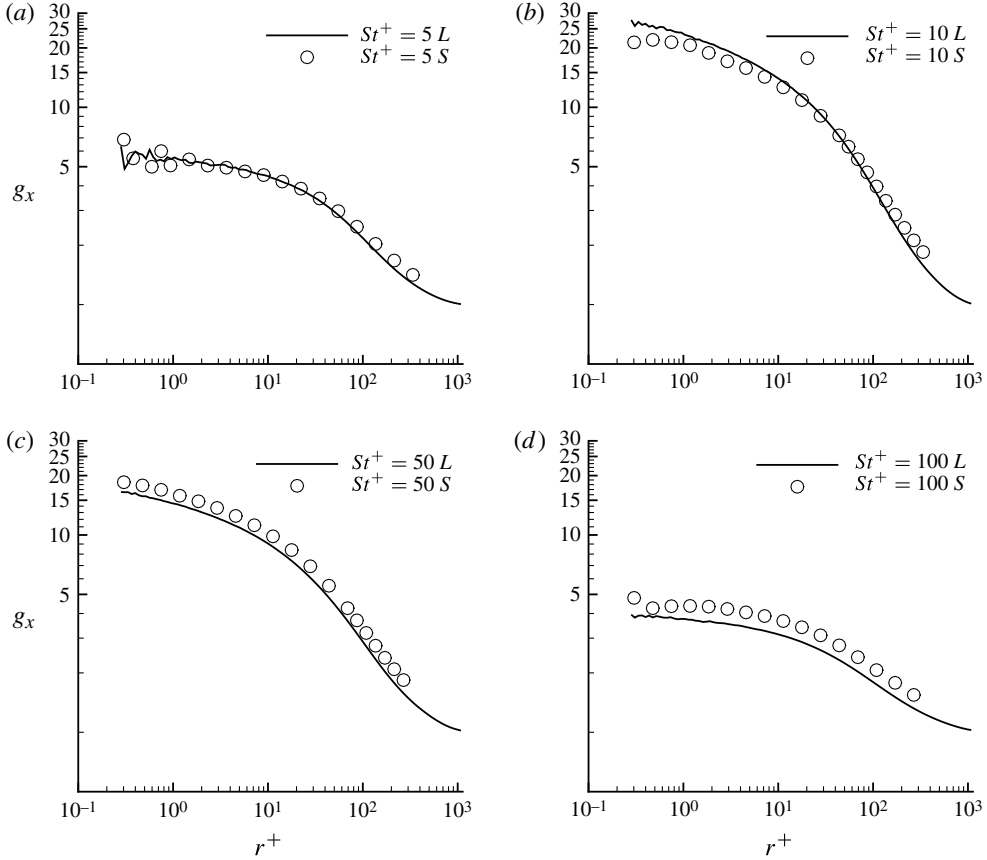
FIGURE 13. ADF in the streamwise direction for four different particle populations in the near-wall region ($y^+ = 1$).

60 wall units, consistent with the concept that heavy particles tend to filter small-scale turbulent motions. The particle inertia tends to filter the high temporal frequency of the fluid velocity fluctuations. As can be understood by the particle equation (2.3), the filter cut-off time scale is of the order of the particle relaxation time τ_p. Since wall turbulence is constituted by spatial–temporal coherent structures, the time scale of velocity fluctuations can be related to the characteristic length scale by means of their typical velocity. Since the friction velocity is the natural choice for the velocity scale in the near-wall region, the particle relaxation time can be easily translated into the length scale Δ of an equivalent spatial filter, leading to $\Delta^+ = U^* \tau_p / \delta_v = St^+$. Hence we expect that, as long as the filter length scale is smaller than the typical distance between velocity streaks δ_s^+, i.e. $\Delta^+ < \delta_s^+$, the particles interact with the coherent structures forming the streaks, yielding $l_c \sim \ell_z$. On the other hand, when $\Delta^+ > \delta_s^+$, the particles feel only a filtered fluid velocity field with a filter width larger than the streak spacing. Under these conditions, the particle structures should scale with Δ^+, as the distance between the filtered velocity streaks.

In the small-box simulation, particle structures are very regularly spaced and highly correlated in the spanwise direction, as understood by the clear oscillating behaviour of the ADF at large separation scale (see insets) and appreciated from the instantaneous configuration of figure 5. The order is much reduced for the large
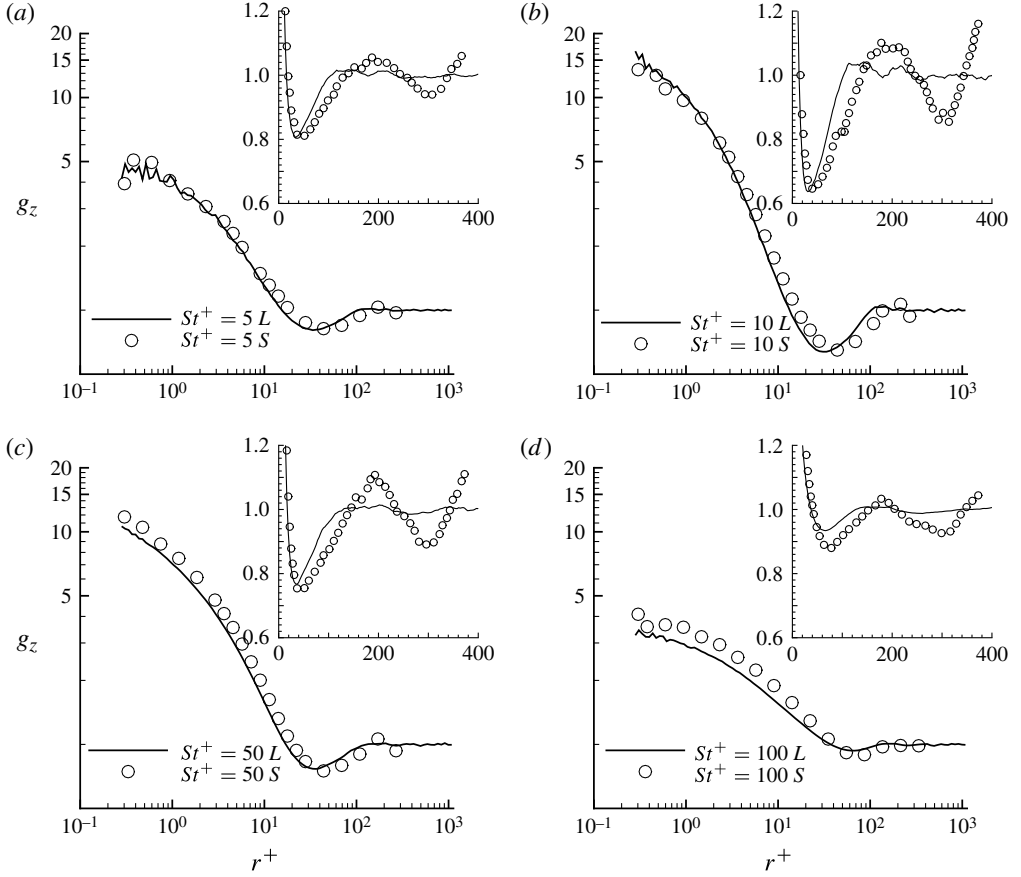
FIGURE 14. ADF in the spanwise direction for four different particle populations in the near-wall region ($y^+ = 1$).

domain, where, at separations larger than 100 wall units, the particle pair distribution achieves an almost uniform state. Besides the large-scale behaviour of the aggregates, the domain size seems to affect also the small-scale features of the particle distribution, at least for sufficiently massive particles. Data at $St^+ = 50$, 100 show increased clustering at small scales in the small domain, as illustrated by the open circles above the solid line in figure 14(b). These findings confirm that the large-scale fluid structures may have a significant influence on particle patterns.

Interestingly, the behaviour at very small scale, $r^+ \simeq 1$, presents some peculiar aspects. The most accumulating particles, $St^+ = 10$, 50, show a probability of finding particle pairs aligned in the streamwise direction more than twice that in the spanwise direction, as can be deduced by the ratio between the values of ADF in the spanwise and streamwise directions. This implies that particle clusters are streamwise aligned even at these very small scales. A different behaviour is experienced by smaller or larger particles, which are more isotropically distributed at these small scales.

The ADF, $g(r, \hat{\boldsymbol{r}}, y)$, can be decomposed into an isotropic component

$$g_0(r, y) = (1/2\pi) \int_0^{2\pi} g(r, \hat{\boldsymbol{r}}(\theta), y) \, d\theta, \tag{3.7}$$
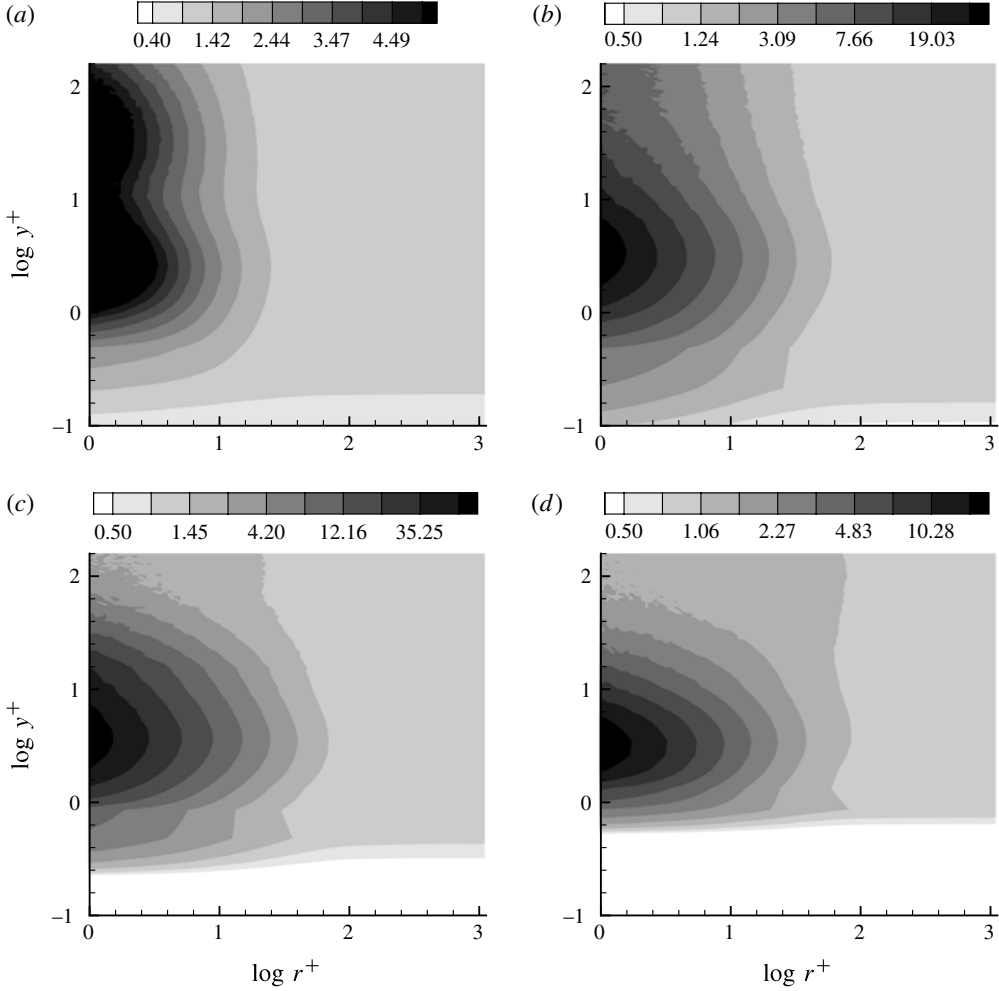
FIGURE 15. Isotropic component of ADF, g_0, for four different Stokes numbers: (*a*) $St^+ = 5$, (*b*) $St^+ = 10$, (*c*) $St^+ = 50$, and (*d*) $St^+ = 100$. Note the different greyscale values for the individual panels.

where θ is the angle between $\hat{\boldsymbol{r}}$ and the spanwise direction, and an anisotropic component. Focusing on the large domain, the isolines of the RDF g_0, i.e. the isotropic component of the ADF, are shown in figure 15 for several particle populations in the (r^+, y^+) plane. This kind of plot allows the behaviour of the clustering process to be examined as a function of the wall-normal location y^+. Overall, from figure 15, peak clustering occurs for particles with $St^+ = 10$, 50, which are also those most subjected to turbophoresis. Recalling that, given its normalization, the ADF does not depend directly on local concentration, a genuine correlation between wall accumulation and segregation emerges.

Despite the fact that the maximum accumulation takes place at the wall, particles tend to achieve maximum clustering a little further away at $y^+ \simeq 3$ (see figure 15), where the local concentration level is already lower by more than one order of magnitude than right at the wall (see figure 7). The viscous sublayer and lower buffer

layer are clearly locations where the highest clustering is achieved, as a consequence of flow inhomogeneity and fluid structure population.

Particles with $St^+ = 10$, 50 exhibit large values of g_0 (30 and 60, respectively) at separations of the order of one wall unit (see figure 15), implying that their collision rate could be enhanced by a factor of 30–60 compared to that of an uncorrelated distribution with the same local concentration. For lighter particles, namely $St^+ = 5$, a second peak develops in g_0. This second peak occurs in the lower outer region where the local Kolmogorov time scale ($\tau_\eta = \sqrt{\nu/\varepsilon}$, with ε the turbulent kinetic energy dissipation) matches the relaxation time, leading to a Kolmogorov–Stokes number $St_\eta = \tau_p/\tau_\eta$ of the order of unity. This behaviour is consistent with the observation derived from homogeneous flows, where particles at $St_\eta \simeq 1$ are known to be the most prone to small-scale clustering. This effect cannot be observed for heavier particles because their Kolmogorov–Stokes numbers exceed unity everywhere in the channel. We stress that the near-wall clustering peak occurs in fact independently of the local Kolmogorov–Stokes number, being essentially associated with turbophoresis.

To study the geometry of the particle patterns in more detail, the anisotropy indicator (Casciola *et al.* 2007)

$$A(r, y) = \sqrt{\frac{\int (g(r, \theta, y) - g_0(r, y))^2 \, \mathrm{d}\theta}{\int g_0^2(r, y) \, \mathrm{d}\theta}} \tag{3.8}$$

is evaluated and plotted in figure 16. The anisotropy indicator $A(r, y)$ is an increasing function of the anisotropy level of the particle distribution (zero corresponds to completely isotropic conditions). Both heavy (ballistic) and very light (purely Lagrangian) particles are expected eventually to reach a uniform and isotropic distribution. Consistently the strongest anisotropy occurs for intermediate Stokes numbers, of the order of $St^+ = 10$, 50. For all populations that we have presently considered, the maximum level of anisotropy is reached in the viscous sublayer at $y^+ \simeq 2.5$ and separation of ~ 30 wall units, where the anisotropy component exceeds the isotropic one, leading to $A = 2.5$ for particles with $St^+ = 50$. The separation of 30 wall units compares well with the transverse characteristic length of particle patterns l_c, confirming that the streaky structures are the origin of the measured anisotropy. Below this length scale, the ADF tends to decrease the directionality. However, a substantial level of anisotropy is retained even at $r^+ = 1$ in the viscous sublayer for particles with $St^+ = 10$, 50 displaying $A \simeq 0.8$. As a general trend, isotropy tends to be recovered by all particle populations for fixed separation r^+ moving from the wall towards the bulk of the flow. It was found by Gualtieri *et al.* (2009) that, in particle-laden homogeneous shear flow, the anisotropy level of particle clustering increases with decreasing separation owing to the presence of mean shear. For the present configuration, this behaviour is recovered in the log layer, e.g. $y^+ = 100$, where the anisotropy level is found to increase for all particle populations reducing the separation distance r^+ down to small scales. This is not surprising since homogeneous shear flow is known to reproduce the most relevant feature of the turbulent dynamics in the log layer (see e.g. Casciola *et al.* 2005).

As stated before, the behaviour of $g_0(r)$ near the origin is singular, $g_0(r) \propto r^{-\alpha}$, with $\alpha > 0$. The probability of finding a pair of particles at small separation is thus an increasing function of the exponent, i.e. the larger α, the more intense is the clustering at small scales. In figure 17(b) the exponent α is plotted as a function of the wall-normal distance. The most evident feature of the plot is the well-defined
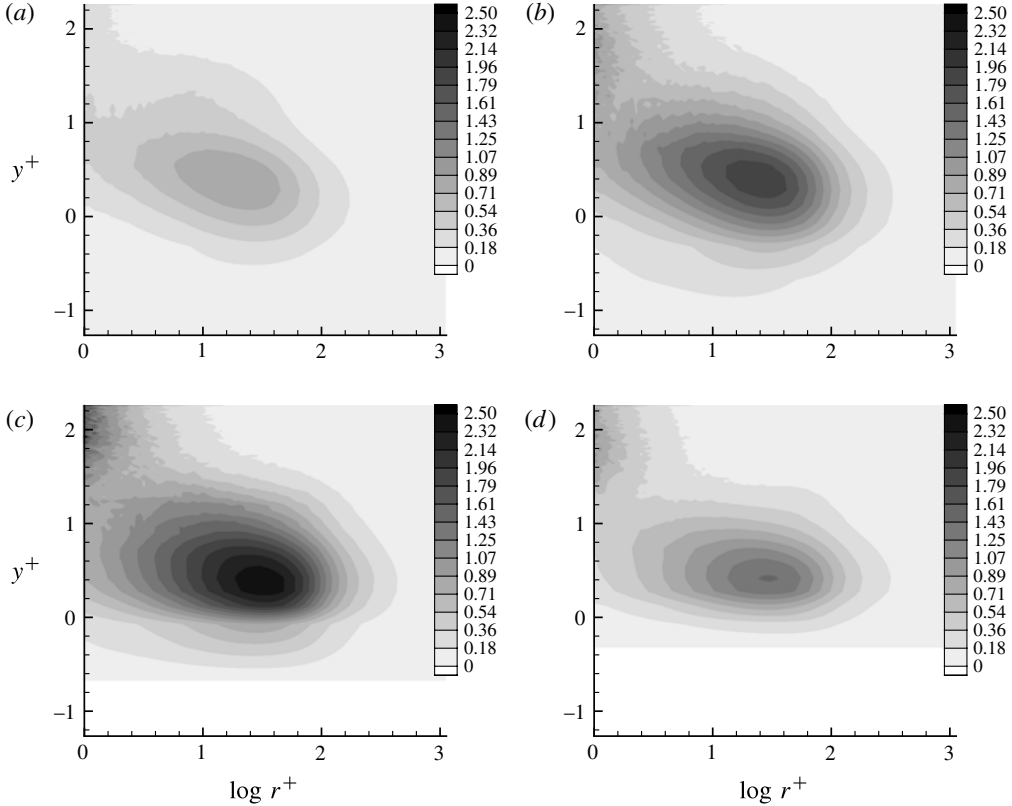
FIGURE 16. Anisotropy indicator of ADF for four different particle populations: (*a*) $St^+ = 5$, (*b*) $St^+ = 10$, (*c*) $St^+ = 50$, and (*d*) $St^+ = 100$.

maximum of α occurring in the viscous sublayer ($y^+ = 3$–5) for most accumulating particles. The values of α exhibited in the bulk of the flow ($y^+ > 100$) are consistent with the values found for homogeneous conditions, where the relevant parameter is the Kolmogorov–Stokes number $St_\eta = \tau_p/\tau_\eta$ ($\tau_\eta = \eta^2/\nu$) – see Bec *et al.* (2007) and Gualtieri *et al.* (2009). In particular, particles with $5 \leqslant St^+ \leqslant 50$ are characterized by a Kolmogorov–Stokes number of the order of unity in this outer region (see figure 17*a*), and display $\alpha \simeq 0.5$. Interestingly, $St^+ = 100$ particles tend to achieve a uniform distribution (small α) in the bulk owing to their ballistic behaviour ($St_\eta = 5$–10). We stress that the maxima of the exponent in the viscous sublayer cannot be explained in terms of the local Kolmogorov–Stokes number, at least for particles with $St^+ > 10$ characterized by $2 < St_\eta < 20$. In particular, most wall-accumulating particles, $St^+ = 10$, 50, show the highest exponents $\alpha \simeq 0.8$. A unit value of the exponent α would imply that the particle clusters become one-dimensional lines in the *x*–*z* plane. This happens for particles with $St^+ = 10$, 50, which distribute in very narrow structures that are indeed almost one-dimensional lines in the *x*–*z* plane. As shown by the ADF (figures 12–14) and by the anisotropy indicator A (figure 16), these aggregates are close to straight lines, oriented in the streamwise direction, as apparent in the visualization of figure 5.
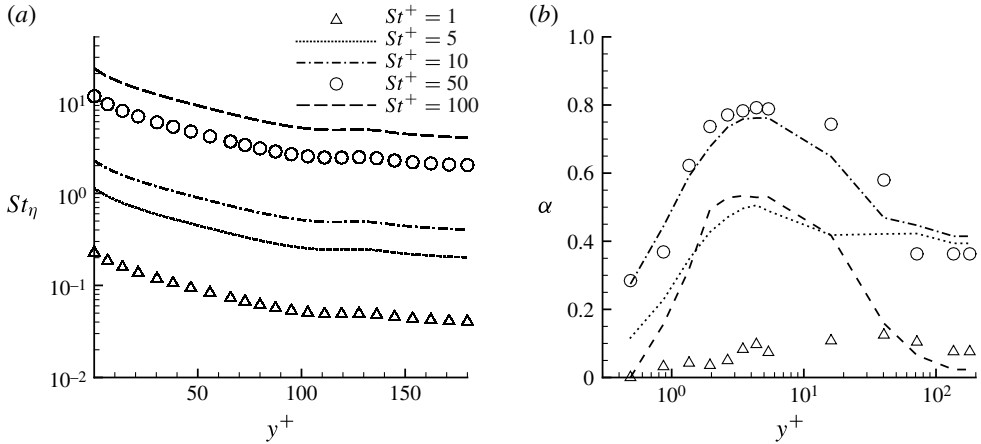
FIGURE 17. (*a*) Kolmogorov–Stokes number St_η along the wall-normal direction. (*b*) Co-dimension of fractal dimension that characterizes small-scale clustering.

4. Conclusion

We perform DNS of a particle-laden channel flow at friction Reynolds number $Re_\tau = 180$ in two computational domains: a standard size and a very large computational domain. Several point particle populations with friction Stokes number ranging from pure tracers, $St^+ = 0$, to heavy particles, $St^+ = 100$, have been considered. Maximum wall accumulation due to turbophoresis is observed at Stokes numbers of the order of $St^+ = 10$–50 when the particle Stokes time matches the turbulence time scale of the buffer layer. Comparing particle statistics between the large and the small domains, a surprising increase of wall particle concentration is found in the large domain, up to 20 % difference with respect to the small domain. On the other hand, the single-point fluid and particle velocity probability distributions are found to be substantially unaffected by domain truncation. The analysis of the instantaneous configurations shows that the mean particle concentration is composed of an ensemble of strongly localized instantaneous patterns, which are strongly influenced by the spatial structure of the advecting fluid velocity field. Insufficient domain dimensions by inducing an artificial correlation in the velocity field lead to blocking effects of the particle aggregates, which show an increased level of artificial order in the small domain. Based on the present results, we believe that the length of particle streaks is of the order of 10^3 inner units, i.e. much larger than the velocity streaks. The apparent relation between mean wall accumulation and particle localization effects motivates the analysis of more sophisticated statistical observables like the radial (RDF) and the angular (ADF) distribution functions. These tools allow us to analyse the intensity and the geometry of the clustering as a function of the scale and of the wall-normal distance. The typical streamwise extent of the particle aggregates is estimated to be 500–1000 wall units. For particles with $St^+ \leqslant 50$, the typical transverse distance of the particle aggregates is determined by the spanwise correlation length of the wall-normal velocity, while heavier particles display larger separations. This effect can be understood by translating the delay time of the particle response, τ_p, into a related filter length Δ operating on the advecting fluid velocity field.

Small-scale clustering can be quantified by the singularity exponent α of the RDF. Typical values found in homogeneous turbulence are of the order of 0–0.7 depending

on the Kolmogorov–Stokes number, with a maximum attained for $St_\eta \simeq 1$. For the present flow case, this kind of behaviour is recovered in the outer part of the flow, as expected. The peculiar aspect is the correlation between turbophoresis and small-scale clustering: the singularity exponent attains its maximum as a function of wall-normal distance in the viscous sublayer where the local Kolmogorov–Stokes number greatly exceeds unity, with most accumulating particles, $St^+ = 10$, 50, displaying the largest exponents. The closeness of this exponent to one, $\alpha \simeq 0.8$, and the high level of directionality (anisotropy) of these clusters also at small scales imply that the particles in the wall-parallel plane tend to segregate in quasi-one-dimensional straight lines almost aligned with the streamwise direction. The reason for this behaviour lies in the dynamics of turbophoresis and is better understood by addressing the steady state. It can be shown that, in order to balance the turbophoretic drift of the particles towards the wall, it is strictly necessary that the particles localize in regions of slow wall-departing fluid. This causes the streamwise-oriented quasi-one-dimensional patterns we have described in detail in the present paper.

The combination of wall accumulation leading to large particle concentration near the wall with strong clustering and anisotropy of the particle aggregates is expected to crucially enhance the collision rate between particles, and the actual collision models need to be improved to capture these effects.

Acknowledgements

REFERENCES

DEL ÁLAMO, J. & JIMÉNEZ, J. 2003 Spectra of the very large anisotropic scales in turbulent channels. *Phys. Fluids* **15**, L41.

AYYALASOMAYAJULA, S., GYLFASON, A., COLLINS, L. R., BODENSCHATZ, E. & WARHAFT, Z. 2006 Lagrangian measurements of inertial particle accelerations in grid generated wind tunnel turbulence. *Phys. Rev. Lett.* **97** (14), 144507.

BALACHANDAR, S. & EATON, J. K. 2010 Turbulent dispersed multiphase flow. *Annu. Rev. Fluid Mech.* **42**, 111–133.

BEC, J., BIFERALE, L., CENCINI, M., LANOTTE, A., MUSACCHIO, S. & TOSCHI, F. 2007 Heavy particle concentration in turbulence at dissipative and inertial scales. *Phys. Rev. Lett.* **98** (8), 84502.

CALZAVARINI, E., CENCINI, M., LOHSE, D. & TOSCHI, F. 2008 Quantifying turbulence-induced segregation of inertial particles. *Phys. Rev. Lett.* **101** (8), 84504.

CANUTO, C., HUSSAINI, M. Y., QUARTERONI, A. & ZANG, T. A. 1988 Springer.

CAPORALONI, M., TAMPIERI, F., TROMBETTI, F. & VITTORI, O. 1975 Transfer of particles in nonisotropic air turbulence. *J. Atmos. Sci.* **32** (3), 565–568.

CASCIOLA, C. M., GUALTIERI, P., JACOB, B. & PIVA, R. 2005 Scaling properties in the production range of shear dominated flows. *Phys. Rev. Lett.* **95** (2), 024503.

CASCIOLA, C. M., GUALTIERI, P., JACOB, B. & PIVA, R. 2007 The residual anisotropy at small scales in high shear turbulence. *Phys. Fluids* **19**, 101704.

CERBELLI, S., GIUSTI, A. & SOLDATI, A. 2001 ADE approach to predicting dispersion of heavy particles in wall-bounded turbulence. *Intl J. Multiphase Flow* **27** (11), 1861–1879.

CHEVALIER, M., SCHLATTER, P., LUNDBLADH, A. & HENNINGSON, D. S. 2007 SIMSON: a pseudo-spectral solver for incompressible boundary layer flows. *Tech. Rep.*, TRITA-MEK 2007:07. KTH Mechanics, Stockholm.

COLEMAN, S. W. & VASSILICOS, J. C. 2009 A unified sweep–stick mechanism to explain particle clustering in two- and three-dimensional homogeneous, isotropic turbulence. *Phys. Fluids* **21**, 113301.

EATON, J. K. & FESSLER, J. R. 1994 Preferential concentration of particles by turbulence. *Intl J. Multiphase Flow* **20**, 169–209.

ELPERIN, T., KLEEORIN, N. & ROGACHEVSKII, I. 1996 Self-excitation of fluctuations of inertial particle concentration in turbulent fluid flow. *Phys. Rev. Lett.* **77** (27), 5373–5376.

FESSLER, J. R., KULICK, J. D. & EATON, J. K. 1994 Preferential concentration of heavy particles in a turbulent channel flow. *Phys. Fluids* **6**, 3742.

GERASHCHENKO, S., SHARP, N. S., NEUSCAMMAN, S. & WARHAFT, Z. 2008 Lagrangian measurements of inertial particle accelerations in a turbulent boundary layer. *J. Fluid Mech.* **617**, 255–281.

GOTO, S. & VASSILICOS, J. C. 2008 Sweep–stick mechanism of heavy particle clustering in fluid turbulence. *Phys. Rev. Lett.* **100** (5), 54503.

GUALTIERI, P., PICANO, F. & CASCIOLA, C. M. 2009 Anisotropic clustering of inertial particles in homogeneous shear flow. *J. Fluid Mech.* **629**, 25–39.

KAFTORI, D., HETSRONI, G. & BANERJEE, S. 1995a Particle behaviour in the turbulent boundary layer. I. Motion, deposition, and entrainment. *Phys. Fluids* **7** (5), 1095–1106.

KAFTORI, D., HETSRONI, G. & BANERJEE, S. 1995b Particle behaviour in the turbulent boundary layer. II. Velocity and distribution profiles. *Phys. Fluids* **7**, 1107.

KLINE, S. J., REYNOLDS, W. C., SCHRAUB, F. A. & RUNSTADLER, P. W. 1967 The structure of turbulent boundary layers. *J. Fluid Mech.* **30** (4), 741–773.

LI, Y., MCLAUGHLIN, J. B., KONTOMARIS, K. & PORTELA, L. 2001 Numerical simulation of particle-laden turbulent channel flow. *Phys. Fluids* **13**, 2957.

MARCHIOLI, C. & SOLDATI, A. 2002 Mechanisms for particle transfer and segregation in a turbulent boundary layer. *J. Fluid Mech.* **468**, 283–315.

MARCHIOLI, C., SOLDATI, A., KUERTEN, J. G. M., ARCEN, B., TANIERE, A., GOLDENSOPH, G., SQUIRES, K. D., CARGNELUTTI, M. F. & PORTELA, L. M. 2008 Statistics of particle dispersion in direct numerical simulations of wall-bounded turbulence: results of an international collaborative benchmark test. *Intl J. Multiphase Flow* **34** (9), 879–893.

MAXEY, M. R. & RILEY, J. J. 1983 Equation of motion for a small rigid sphere in a nonuniform flow. *Phys. Fluids* **26**, 883.

MEHLIG, B., WILKINSON, M., DUNCAN, K., WEBER, T. & LJUNGGREN, M. 2005 Aggregation of inertial particles in random flows. *Phys. Rev.* E **72** (5), 051104.

MONCHAUX, R., BOURGOIN, M. & CARTELLIER, A. 2010 Preferential concentration of heavy particles: a Voronoï analysis. *Phys. Fluids* **22**, 103304.

MOSER, R. D., KIM, J. & MANSOUR, N. N. 1999 Direct numerical simulation of turbulent channel flow up to $Re_\tau = 590$. *Phys. Fluids* **11**, 943.

NIÑO, Y. & GARCIA, M. H. 1996 Experiments on particle turbulence interactions in the near-wall region of an open channel flow: implications for sediment transport. *J. Fluid Mech.* **326**, 285–319.

PAN, Y. & BANERJEE, S. 1996 Numerical simulation of particle interactions with wall turbulence. *Phys. Fluids* **8**, 2733.

PICANO, F., SARDINA, G. & CASCIOLA, C. M. 2009 Spatial development of particle-laden turbulent pipe flow. *Phys. Fluids* **21** (9), 3305.

PICCIOTTO, M., MARCHIOLI, C. & SOLDATI, A. 2005 Characterization of near-wall accumulation regions for inertial particles in turbulent boundary layers. *Phys. Fluids* **17**, 098101.

REEKS, M. W. 1983 The transport of discrete particles in inhomogeneous turbulence. *J. Aerosol Sci.* **14** (6), 729–739.

RIGHETTI, M. & ROMANO, G. P. 2004 Particle–fluid interactions in a plane near-wall turbulent flow. *J. Fluid Mech.* **505**, 93–121.

ROUSON, D. W. I. & EATON, J. K. 2001 On the preferential concentration of solid particles in turbulent channel flow. *J. Fluid Mech.* **428**, 149–169.

SARDINA, G., PICANO, F., SCHLATTER, P., BRANDT, L. & CASCIOLA, C. M. 2011 Large scale accumulation patterns of inertial particles in wall-bounded turbulent flow. *Flow Turbul. Combust.* **86** (3–4), 519–532.

SHOTORBAN, B. & BALACHANDAR, S. 2006 Particle concentration in homogeneous shear turbulence simulated via Lagrangian and equilibrium Eulerian approaches. *Phys. Fluids* **18**, 065105.

SQUIRES, K. & EATON, J. 1991 Measurements of particle dispersion obtained from direct numerical simulations of isotropic turbulence. *J. Fluid Mech.* **226**, 1–35.

SUNDARAM, S. & COLLINS, L. R. 1997 Collision statistics in an isotropic particle-laden turbulent suspension. Part 1. Direct numerical simulations. *J. Fluid Mech.* **335**, 75–109.

TOSCHI, F. & BODENSCHATZ, E. 2009 Lagrangian properties of particles in turbulence. *Annu. Rev. Fluid Mech.* **41**, 375–404.

WANG, L. P. & MAXEY, M. R. 1993 Settling velocity and concentration distribution of heavy particles in homogeneous isotropic turbulence. *J. Fluid Mech.* **256**, 27–68.

YOUNG, J. & LEEMING, A. 1997 A theory of particle deposition in turbulent pipe flow. *J. Fluid Mech.* **340**, 129–159.